# Coupling Anionic Oxygen Redox with Selenium for Stable High-voltage Sodium Layered Oxide Cathodes

Zhichen Xue [a], Neha Bothra [b], Dechao Meng [a], Guangxia Feng [c], Yuqi Li [c], Tony Cui [c], Hongchang Hao [d], Sang-Jun Lee [a], Yijin Liu [e], Michal Bajdich [b,*], Jagjit Nanda [c,d,*], Xueli Zheng [c,d*]

[a.] Stanford Synchrotron Radiation Lightsource, SLAC National Accelerator Laboratory, Menlo Park, CA, USA
[b.] SUNCAT Center for Interface Science and Catalysis, SLAC National Accelerator Laboratory, Menlo Park, CA, USA
[c.] Materials Science and Engineering, Stanford University, Stanford, California 94305, USA
[d.] Applied Energy Division, SLAC National Accelerator Laboratory, Menlo Park, CA, USA
[e.] Walker Department of Mechanical Engineering, The University of Texas at Austin, Austin, TX, USA

**Keywords**: materials science； sodium ion battery; layered oxide cathode; anion redox chemistry

**Abstract**

Utilizing anion redox reaction is crucial for developing the next generation of high-energy density, low-cost sodium-ion batteries. However, the irreversible oxygen redox reaction in Na-ion layered cathodes, which leads to voltage fading and reduced overall lifespan, has hindered their practical application. In this study, we incorporated selenium as a synergistic redox active center of oxygen to improve the stability of Na-ion cathodes. Our redesigned cathode maintains stable voltage by demonstrating reversible oxygen redox while significantly suppressing the redox activity of manganese. The anionic redox contribution capacity of the selenium-doped $Na_{0.6}Li_{0.2}Mn_{0.8}O_2$ cathode remains as high as 84% after 50 cycles, while the pristine $Na_{0.6}Li_{0.2}Mn_{0.8}O_2$ cathode experiences a reduction to 39% of its initial capacity. Our X-ray photoelectron spectroscopy data and computational analysis further revealed that selenium doping participates in redox as $Se^{+4/5}$ which stabilizes the charged state and increases the energy step for O-O dimerization, thus improving the stability and lifespan of $Na_{0.6}Li_{0.2}Mn_{0.8}O_2$ cathodes. Our findings highlight the potential of redox coupling design to address the issue of voltage fade caused by irreversible anionic redox.

## Introduction

Sodium-ion (Na-ion) batteries have gained significant attention as a sustainable solution for addressing resource concerns associated with lithium-based energy storage [1]. Using abundant and cost-effective sodium raw materials has been a key advantage. However, the practical implementation of Na-ion batteries has been hindered by their lower specific energy than lithium-ion batteries due to their heavier nature and the less-reducing potential of sodium. To enhance the market competitiveness of Na-ion batteries, improving the cell-level specific energy density by developing high-voltage Na-ion cathodes is urgently needed[2]. Utilizing anion redox reaction during the desodiation of layered oxide cathodes offers a promising opportunity for achieving high-energy-density Na-ion batteries as it allows for the storage of charges on both transition metal cations and oxygen anions [3-6].

Typically, when charged to high voltage, the oxidation of $O^{2-}$ to $O^{n-}$ (where $n < 2$, resembling peroxide or superoxide), and even the undesirable oxidation of some oxygen to a gaseous state, leads to its escape from lattice [7, 8]. This causes interlayered lattice degradation, along with the evolution of the superlattice from ordered to disordered [9, 10]. The released oxygen reacts with the electrolyte, consuming it and degrading the cathode-electrolyte interface. Importantly, this process lowers the oxidation states of transition metal ions, influencing the evolution of redox centers and altering redox behavior, with anionic redox reactions decreasing at high voltages and cationic redox reactions increasing at low voltages, leading to voltage decay [11, 12].

Despite the difficulties in utilizing anion redox reactions in Na-ion cathodes, recent years have seen substantial progress in exploring and optimizing Na-ion layered cathodes to effectively harness these reactions [13, 14]. Wang and colleagues demonstrated that the strong covalent Cu–(O–O) bonding can effectively suppress excessive oxygen oxidation and irreversible cation migration, leading to the design of a P2-$Na_{0.8}Cu_{0.22}Li_{0.08}Mn_{0.67}O_2$ cathode with enhanced reversibility of O-O dimerization [15]. Similarly, Yao and coworkers have integrated a strategy combining high-entropy component design with superlattice stabilization to extend the cycle life and improve anion redox reversibility [16]. Inhibiting the loss of lattice oxygen requires reducing O-O

dimerization and decreasing the extent of anion oxidation. However, reducing the reaction extent means sacrificing the energy density provided by anion redox. Therefore, maximizing energy density while carefully controlling the redox reaction to maintain stability and reversibility in Na-ion cathodes would be ideal. Utilizing electrochemically active element doping or substitution presents a potential solution to address this challenge effectively [17].

Selenium (Se) has been demonstrated to possess electrochemical redox activity at high voltage and could potentially enhance the stability of anionic redox as reported [18-20]. Herein, we focus on $Na_{0.6}Li_{0.2}Mn_{0.8}O_2$ (NLMO), as a low-cost and high-capacity Na-ion cathode material leveraging reversible anionic redox [3, 4]. In the NLMO material, anionic oxidation occurs with charge transfer during the initial charging process. During the first discharge, anionic redox takes place above 3.8V. Cationic redox occurs below 3.8V, as indicated in **Fig. 1A**. With cycling, the release of oxygen leads to the reduction of manganese (Mn), which increasingly contributes to charge transfer [11]. This transition reduces the anionic capacity and increases the cationic contribution, resulting in voltage decay (**Fig.1B**). To improve the reversibility of oxygen redox, we designed Se-doped NLMO (NLMO-Se). For NLMO-Se, the charge transfer mechanism during the first charge and discharge is similar to that of NLMO (**Fig. 1C**). The electrochemical redox activity of Se allows it to participate in redox reactions between the 4+ and 5+ states. The introduction of Se increases the energy barrier for O-O dimerization, enhancing the reversibility of anionic redox on the NLMO cathode and curtailing the release of lattice oxygen. Consequently, this reduces the cationic capacity contribution and stabilizes the voltage throughout the cycling process (**Fig. 1D**).

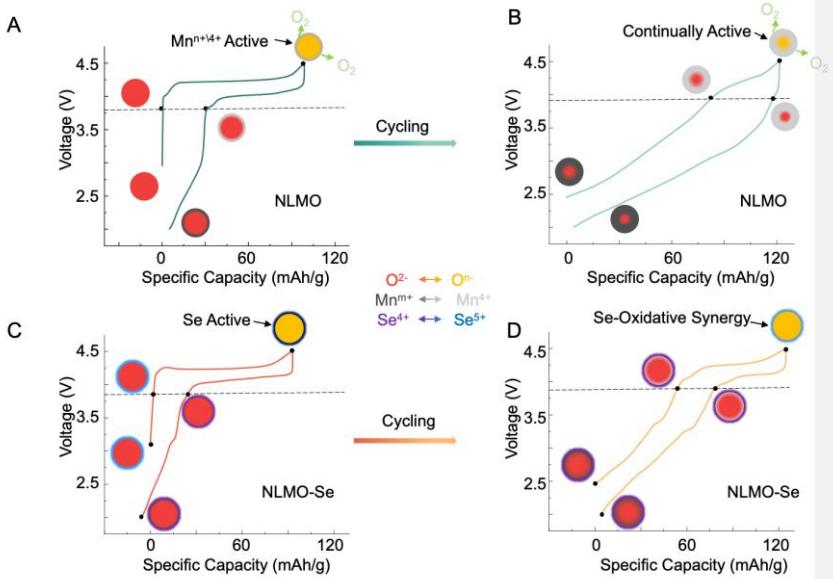


**Fig. 1** Schematic of redox couple evolution in the NLMO and NLMO-Se.

A, B, The redox behavior of Mn and O in NLMO during the initial cycling and continuous cycling. The Mn redox contribution increases with cycling, while O redox contribution decreases.

C, D, The redox behavior of Mn, O, and Se in NLMO-Se during the initial cycling and continuous cycling. Se dopants undergo redox reactions during charge and discharge. This results in less lattice oxygen loss and less Mn being activated during cycling, preserving the redox activity of oxygen anions.

## Results

### Se doped NLMO synthesis and characterization

The NLMO-Se is synthesized by mixing NLMO material with Se metal powder and sintering the mixture in Air at 600°C. To investigate the lattice structure of NLMO and NLMO-Se, we performed X-ray diffraction (XRD) at beamline 11-3, Stanford Synchrotron Radiation Lightsource (SSRL). As shown in Fig. 2A, the synchrotron X-ray diffraction pattern of NLMO reveals prominent peaks consistent with a layered P3-type structure [5, 21], featuring an AABBCC oxygen stacking sequence. Sodium ions occupy the interlayer trigonal prismatic sites formed by the oxygen arrays, aligning with the stacking sequence (A-A, B-B, or C-C). The structural refinement was performed using a Li/Mn-ordered ribbon superlattice model as reported by Gao and his co-workers[9], which

accurately captures the observed diffraction peaks. This superlattice structure plays a pivotal role in stabilizing the anionic redox reactions, as highlighted in previous studies. Notably, the absence of new peaks in NLMO-Se suggests that Se integrates into the lattice as a dopant (**Fig. 2B**). This is corroborated by transmission electron microscopy energy dispersive spectroscopy analysis that indicate a uniform distribution of Se alongside Mn, Na, and O (**Fig. 2C**). Cross-sectional scanning electron microscope energy dispersive spectroscopy line scans show that Se enrichment is on the surface, not penetrating the particle's interior, indicating spatially heterogeneous doping (**Fig. S1**).

To validate the experimental observations, we have also performed a detailed DFT computational study of the NLMO and NLMO-Se systems under the discharged (Na-rich, sodatiated) and charged (Na-poor, desodatiated) conditions. We adapted the discharged P3-NLMO supercells from the study by Gao et al. [5]. Our optimization of the charged supercells also resulted in the P3-NLMO configuration, as reported in the same study. Our calculated electronic states of Mn agree well with the previous in-depth studies having Mn in the +4 state [5, 22, 23]. Comparison of Bader charges of the charged versus the discharged state of NLMO and NLMO-Se (**Fig. S2**) reveal the dominant role of anion oxidation mechanism (via $O^{2-}$) while the oxidation states of Mn (+4), Na (+1) and Li (+1) remain largely intact. Se trace doping at the experimental level of 1%(wt) was simulated via single Se atom substitution in the place of Mn atom in the supercell (**Table S1**).

Results of Se-doping energetics are summarized in the bars plot (**Fig. 2E)** comparing the formation energies of NLMO-Se, computed under oxidizing conditions (See **Fig. S3** for formation energies under reducing synthesize conditions), for both discharged and charged states. Only Mn and Li sites exhibit relatively favorable Se-doping energies, with exothermic values of -0.09 and -0.87 eV, respectively, under charged oxidizing conditions, which is however less accessible under discharged oxidizing conditions. Notably, under reducing conditions, Se can also act as an anion (-2 state), replacing oxygen (**Fig. S3**). The most preferred locations for the considered Se doping are highlighted in **Fig. 2D.** Overall, Se doping at the Mn site in the +4 oxidation is the most favored configuration. X-ray photoelectron spectroscopy (XPS)

analysis of the Se 3p region confirms that selenium is in the +4 oxidation state (**Fig. S4**).

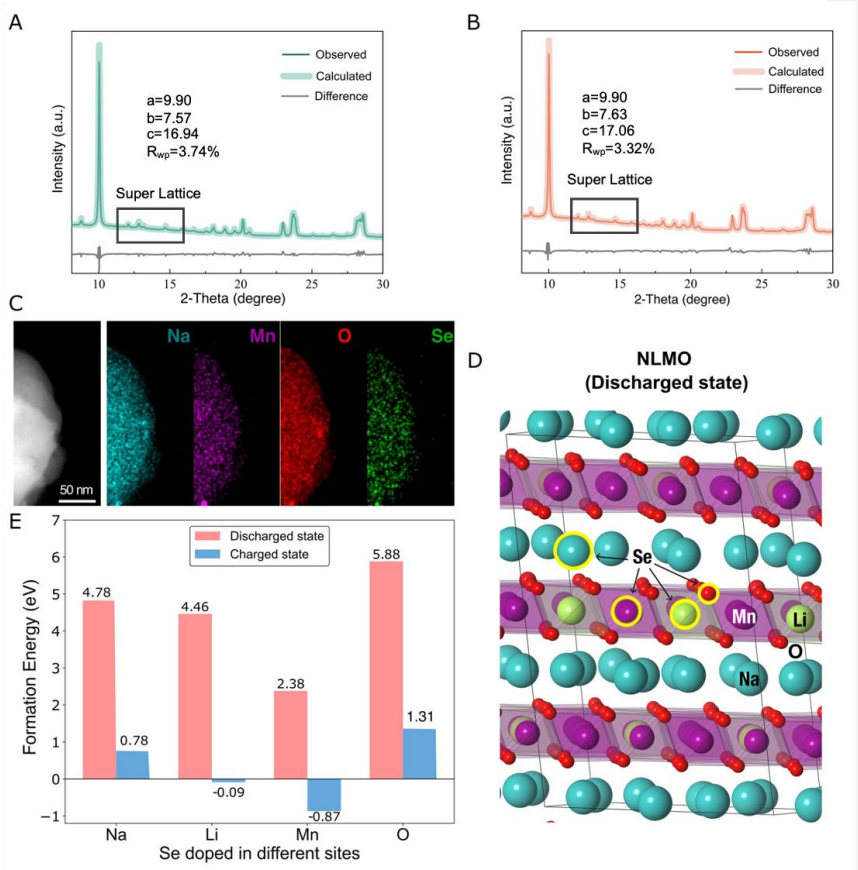


**Fig. 2** Structural characterization of NLMO and NLMO-Se cathodes and energetics of NLMO-Se.
Synchrotron X-ray diffraction pattern (λ = 0.976 Å) of NLMO (A) and NLMO-Se (B).
C, Scanning transmission electron microscopy image and energy dispersive X-ray spectroscopy maps of NLMO-Se.
D, DFT calculated energetics of Se substitution scenarios under oxidizing conditions (w.r.t to binary oxides) for discharged (red) and charged (blue).
E, Computed crystal structure of the doping in NLMO-Se. The yellow-circled one shows the most favorable/stable Se doping locations for each element.

**Electrochemical performance of NLMO and NLMO-Se**

The comparative electrochemical performance evaluation of NLMO and NLMO-Se is depicted in **Fig 3**. Cells using NLMO and NLMO-Se cathodes are

first cycled within the voltage range of 3.5V to 4.5V versus $Na^+/Na$ (**Fig. 3A** and **Fig. 3D**). It is evident that NLMO-Se possesses superior anionic redox reversibility and stability. The initial Coulombic efficiencies for the pristine NLMO and selenium-doped NLMO are 63% and 77%, respectively. This improvement is due to Se doping reducing the release of lattice oxygen, which can otherwise lead to irreversible capacity loss. Additionally, the reduction in oxygen release lessens the potential for side reactions with the electrolyte, further contributing to the enhanced Coulombic efficiency. This stabilization of the oxygen redox reduces non-reversible capacity loss and improves the overall cycling stability of the material. After 50 cycles, the selenium-doped cathode retains an impressive 84% of its reversible anionic redox, whereas the pristine cathode shows a reduction to only 39% of its initial capacity. **Fig. 3B** and **Fig. 3E** display the charge-discharge profiles of NLMO and NLMO-Se across the full voltage window of 2-4.5V versus $Na^+/Na$. It is observed that the high-voltage anionic redox platform of the NLMO material gradually diminishes, with an increasing cationic contribution below 3.5V, leading to a voltage decay. In contrast, NLMO-Se maintains stable and reversible electrochemical charge-discharge curves. **Fig. 3C** and **Fig. 3F** document the dQ/dV plots for both samples, revealing that the peak corresponding to the anionic redox of NLMO at 4.4V declines progressively, while the peak for NLMO-Se shows only a gradual reduction. The cyclic voltammetry (CV) curves, shown in **Fig. S5**, corroborate this behavior. Moreover, severe peak shifting in the CV curves for NLMO is attributed to lattice destruction and hindered ion transport, whereas polarization in NLMO-Se is comparatively subdued. This increase in cationic redox activity and the decrease in anionic redox activity contribute to discharge voltage decay (**Fig. S6**) and a reduction in energy density. As shown in **Fig. 3G**, NLMO and NLMO-Se demonstrate similar specific discharge capacities of around 110 mAh/g, with a slight increase during the initial cycles due to the activation of sodium vacant in the sodium layer of the materials, and negligible capacity decay after 50 cycles. During the activation process, the energy density steadily increases for both NLMO and NLMO-Se, corresponding to the rise in capacity observed in the first few cycles. However, as voltage fade occurs (more details could be accessed in **Fig. S7**), the energy density of

NLMO decreases, while NLMO-Se maintains its stability. Electrochemical impedance spectroscopy **(Fig. S8)** analysis of different cycles reveals that the cell impedance of NLMO continues to increase with cycling, while the polarization increase in NLMO-Se is suppressed.

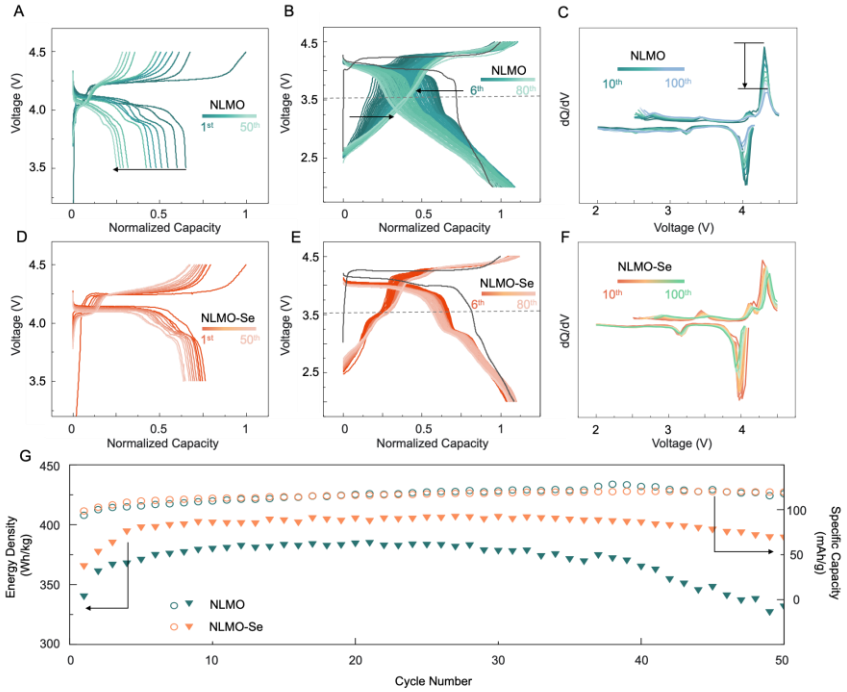


**Fig. 3** The electrochemical performance of NLMO and NLMO-Se.
The charge-discharge profiles of NLMO (A, B) and NLMO-Se (D, E) are depicted under various operating voltage windows. The color gradient from dark to light in these profiles signifies the progression of cycles. The black arrows indicate a decrease in the anionic and an increase in the anionic capacity contribution.
C, F, The dQ/dV plots for NLMO (C) and NLMO-Se (F) illustrate the charge-discharge behavior over cycles 10 to 100.
G, The comparative analysis of the discharge capacity and energy density between NLMO (in green) and NLMO-Se (in orange) is presented (cycled under 25m mA/g current).

**Mechanism on Se doping**

To reveal the mechanism of how Se doping enhanced the electrochemical performance of NLMO, we investigate the changes in cations and anions during cycling. We performed Mn K-edge transmission X-ray microscopy (TXM) X-ray

absorption near edge structure (XANES) to explore the spatial distribution of Mn redox within NLMO and NLMO-Se particles (**Fig. 4A)**. After cycling, the Mn K-edge energy in the NLMO particles was significantly lower compared to that of the NLMO-Se particle. As shown in **Fig. 4B**, the pixel of energy distribution in NLMO particles was concentrated around 5649 eV, whereas in NLMO-Se particles, the energy was mainly concentrated around 6550 eV. It is noteworthy that besides the lower oxidation state, the Mn K-edge energy of NLMO material exhibited a depth-dependent pattern, with lower oxidation states on the surface (**Fig. 4C**). In the case of the NLMO-Se particle, the Mn K-edge energy was higher and did not exhibit a depth-dependent spatial distribution. The Mn K-edge XANES spectra reveal that the as-prepared NLMO and NLMO-Se exhibit negligible differences (**Fig. 4E**). However, after 50 cycles, both NLMO and NLMO-Se exhibit activation of Mn due to their participation in electrochemical reactions. Notably, compared to NLMO-Se, NLMO shows a shift toward lower edge energy. This evidence suggests that the presence of electrochemical-active Se can inhibit the reduction of Mn and participate in the electrochemical redox. The intensity of the TM 3d-O 2p state in the O K-edge fingerprint spectra arises from the O 1s → O 2p dipole transition to unoccupied hybridized states. These states acquire O 2p characteristics through covalent interactions, and the overall oscillator strength is determined by the degree of covalency and the total number of unoccupied d states [24-26]. Phenomenologically, the integrated intensity in this region reflects the oxidative activity of oxygen, as the effective number of holes in oxygen (via TM-O interactions) is proportional to this region. As shown in **Fig. 4F**, the area of this spectral region for the charged NLMO material significantly decreased after the 50$^{th}$ cycle, while the area for the charged NLMO-Se material did not show significant decreases. This implies that after 50 cycles, NLMO-Se also exhibits higher redox activity. Moreover, the peak at 534 eV is

**Commented [ZS1]:** Format here and make it consistent with the rest of the manuscript.

attributed to the characteristic peak of $CO_3^{2-}$, which is a byproduct of the electrolyte decomposition on the cathode surface in reaction with charged electrodes/released oxygen [27-29]. The discharged state of the NLMO material after 50 cycles exhibits a significant presence of $CO_3^{2-}$ on the electrode surface, while NLMO-Se does not. This suggests that by diminishing the release of oxygen, NLMO-Se forms a more robust interface, thereby lessening the degradation of the electrolyte by oxygen.

Similarly, XPS analysis was conducted on cathodes cycling between 3.5 V and 4.5 V versus $Na^+/Na$. The Mn 2p core-level spectra exhibited Mn $2p_{3/2}$ and Mn $2p_{1/2}$ binding energies at 642.5 eV and 653 eV, respectively, indicating the $Mn^{4+}$ state in both pristine NLMO and NLMO-Se [14, 30] (**Fig. S9**). The Mn $2p_{3/2}$ and Mn $2p_{1/2}$ peaks for NLMO after cycling moved to lower binding energies, signifying the presence of a reduced oxidation state. The peaks for NLMO-Se remained unchanged, indicating that the oxidation state of Mn is still in 4+. O1s XPS showed a peak at approximately 530.5 eV, indicating the presence of peroxo-like species (**Fig. S10**) [31-33]. The appearance and disappearance of this component in the spectra of charged and discharged electrodes, respectively, indicate the oxidation of lattice oxygen. It can be observed that by the $20^{th}$ charge cycle, the oxidation of lattice oxygen in the NLMO material is significantly diminished. In contrast, the NLMO-Se still exhibits a distinct peroxo-like species peak, suggesting that it retains higher oxygen redox activity. Furthermore, as depicted in **Fig. S11**, XRD patterns of NLMO exhibit a discernible shift to the left for the (003), (101), and (102) peaks after cycling. In contrast, the XRD pattern of NLMO-Se displays no significant changes before and after cycling.

Taken together, these findings provide strong evidence that the redox coupling strategy can effectively overcome lattice oxygen release and cationic reduction, thereby enhancing the electrochemical stability of the cathode.

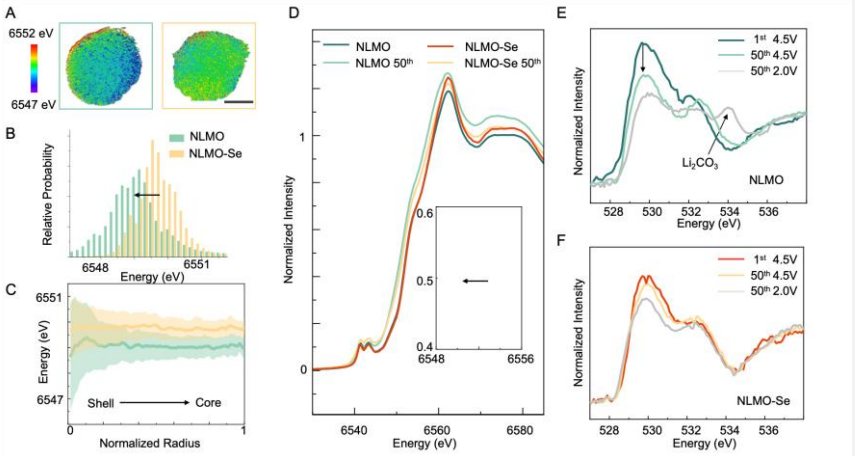


**Fig. 4** Chemical evolution of pristine NLMO and doped NLMO-Se.
A, 2D TXM Mn K-edge energy images of NLMO (left) and NLMO-Se (right) after 50 cycles.
B, statistical probability distribution of edge energy for all pixels.
C, Depth dependent Mn K-edge energy profile.
D, Mn K-edge X-ray absorption spectroscopy (XAS) of NLMO and NLMO-Se, collected at the 1$^{st}$ and 50$^{th}$ cycles, showcasing the evolution of the Mn oxidation state.
E, O K-edge XAS of NLMO, collected from the 1st charged, 50$^{th}$ charged and 50$^{th}$ discharged cathode.
F, O K-edge XAS of NLMO-Se, collected from the 1st charged, 50$^{th}$ charged and 50$^{th}$ discharged cathode.

To further understand the apparent high stability of the NLMO-Se, we have performed additional DFT calculations and analysis of the anion redox stability evaluating lattice oxygen release. Using the above NLMO/NLMO-Se supercells, we have computed the formation energies of oxygen dimers from two lattice oxygens, following the methodology introduced by Kim et al. [*34*]. We selected five distinct pairs of most activated (least stable) oxygen atoms (**Fig. 5A**), using their elevated local magnetic moment as a proxy of their instability. As illustrated by the above Bader charge analysis in **Fig. S2**, the oxidation of oxygen atoms emerges as a primary contributor to their instability, likely leading to the spontaneous formation of oxygen dimers and subsequent $O_2$ release.

A relative comparison of the formation energies before and after Se doping is summarized in **Fig. 5B**. The formation energies of these oxygen pairs were calculated relative to corrected oxygen reference as summarized in the

Methods section. The range of energies for oxygen dimers spans from 1.25 eV to 1.98 eV, while for NLMO-Se, it extends from 2.06 eV to 2.74 eV, indicating a shift towards less favorable dimer formation (i.e. more stable anions) with Se-doping (**Table S2**). Kim et al. [34] reported a similar oxygen vacancy formation energy of ~2.4 eV for NLMO. The comparison of the projected density of states (PDOS) for NLMO and NLMO-Se (insets of **Fig. 5B**) indicates slightly more saturated states near Fermi energy further supporting the suppression of oxidative activity with Se doping. The influence of Se doping on nearest oxygen anions in the NLMO-Se/NLMO system can be directly visualized by the charge density difference plots (**Fig. S12**). Se doping is the most effective in mitigating oxygen dimer formation to nearby oxygen, further supporting the role of surface doping discussed experimentally. Computationally resolved Se oxidation state (**Fig. S13**) is not constant, but evolves between 4.45 to 5.20, for discharged state to the charged state, respectively which also supports the redox role of Se in oxygen anion stabilization.

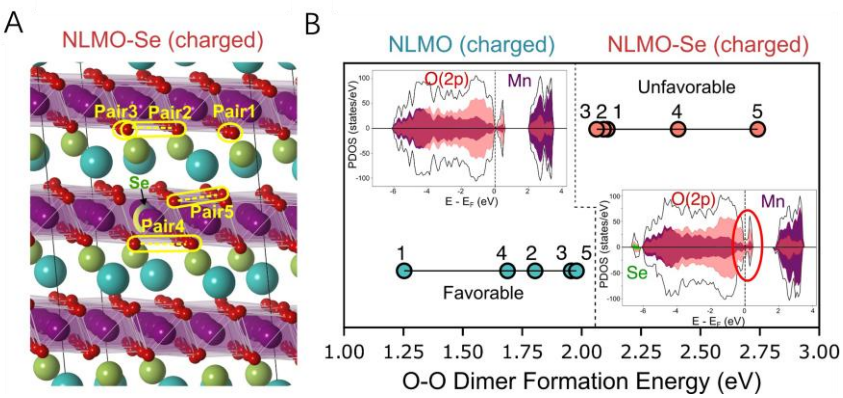


**Fig. 5** The calculation of the formation of selected O-O dimers for the charged NLMO and NLMO-Se.

A, Five selected oxygen pairs are marked with yellow circles, for which O-O dimerization has been computed.

B, Summary of oxygen dimer formation energies before and after doping demonstrates a reduced tendency of Se-doped systems to undergo oxygen-oxygen dimerization. Insets show the PDOS plots highlighting the differences in oxygen's density of states near the Fermi level with a red circle.

**Summary**

In summary, we designed a novel strategy to mitigate voltage fade by incorporating electrochemically active Se in NLMO cathodes as an anion redox synergist. Experimental results show that the Se-doped NLMO cathode exhibits highly reversible anionic redox reactions, reduced Mn redox heterogeneity, and improved structural stability. The role of Se was further investigated computationally and was linked to Se playing a role as the redox-active cation (+4/+5) which stabilizes nearby oxygen ligands, particularly in the charged state. Our work underscores the potential of coupling redox design in tackling lattice oxygen release and anion redox degradation challenges, demonstrating its promising applications in other anion redox cathode materials. With the low cost and scalability of dopants, we believe our strategy paves the way for commercializing energy storage and conversion technologies.

**Materials and Methods**

**Materials Synthesis**

$LiOH{\cdot}H_2O$, $Na_2CO_3$, and $MnO_2$ were thoroughly mixed and calcined at 700°C for 24 hours to produce $Na_{0.6}[Li_{0.2}Mn_{0.8}]O_2$ powder, which is named NLMO. The sample with surface Se doping is prepared by sintering NLMO material and nanoscale selenium powder with a specific mass fraction at 600°C in ambient air for 6 hours, and it is named NLMO-Se.

**Structural Characterization:**

Synchrotron XRD measurements were carried out at the 11-3 beamline of the Stanford Synchrotron Radiation Lightsource. An energy beam of 12.7 keV was utilized for the experiments (with a Rayonix 225 detector), and the LaB6 peak was employed to calibrate the momentum transfer parameter in the diffraction data for each sample (where θ is the scattering angle and λ is the X-ray wavelength). The lab XRD measurements were performed using a Rigaku Ultima IV powder X-ray diffractometer with Cu-Kα radiation (λ=1.54059 Å, 40 kV, 50.0 mA), scanned across a range of 5 to 90 degrees at a scan rate of 0.02 degrees per step. The scanning electron microscope (SEM) images of the cross-sections were acquired using a cross-section preparation device, specifically the CP-100 model from JIT Corporation, which employs two gentle argon (Ar+) focused ion beams for sample preparation. The transmission

electron microscopy energy-dispersive X-ray spectroscopy (TEM EDS) analysis was conducted with a Spectra 300 Transmission Electron Microscope.

**Electrochemical Measurement**

Electrochemical measurements were conducted using coin cells (CR2025) containing sodium metal as the anode, a glass fiber separator, and an electrolyte consisting of 1 M $NaClO_4$ dissolved in a 9:1 mixture of propylene carbonate (PC) and fluoroethylene carbonate (FEC). The cathode comprised 80% active material, 10 wt% carbon, and 10 wt% PVDF binder. The cells were subjected to cycling using a Land battery testing system, and the initial open-circuit voltage of the assembled cell was approximately 2.7 V.

**TXM measurement**

TXM nano-tomography was conducted using the transmission X-ray microscope at beamline 6-2c at the Stanford Synchrotron Radiation Lightsource located at the SLAC National Accelerator Laboratory. This instrument boasts a nominal spatial resolution of approximately 30 nm. For further information on the experimental setup and details refer to the relevant literature[*35*]. Data analysis was carried out using a software package developed in-house at SSRL, known as TXM-Wizard [*36*].

**XAS measurement**

Soft XAS measurements were carried out at SSRL's beamline 10-1. Electrodes were extracted from a standard coin cell with liquid electrolyte and subsequently dried for soft X-ray measurements under ultra-high vacuum conditions. A 600-lines/mm spherical grating monochromator monochromatized the incident beam, set at a 30-degree angle to the sample surface. Simultaneous acquisition of both total fluorescence yield and total electron yield signals took place. To minimize sample exposure to air, $N_2$-filled glove bags were used during sample handling, and measurements were conducted under ultra-high vacuum conditions of approximately $5^{-9}$ Torr. Hard XAS measurements were performed at the 2-2 beamline of the SSRL.

**Theoretical Methods:**

All calculations were carried out with the Vienna Ab-initio Simulation Package (VASP) [*37*] using projector-augmented wave pseudopotentials (PAW) [*38*] to approximate the core electrons. A plane wave basis set with an energy

cutoff of 600 eV was chosen for accurate convergence of bulk structures. Calculations were done on a gamma-centered Monkhorst–Pack grid (*39*) with a k-points of 2x4x2. For the calculation of density of states, a more dense 6x12x6 k-point grid was employed. Energy relaxations were performed until a convergence threshold of $10^{-5}$ eV was achieved, while the forces on individual atoms were converged to 0.02 eV/Å. An effective Hubbard-U (Ueff) value of 2.75 eV [*40*] was introduced for the Mn 3d-electrons to better represent the semiconducting nature of the partially occupied Mn d-band.

Commented [ZS2]: Format issue

Substitutional doping formation energies under the oxidizing and reducing conditions are calculated relative to the corresponding and metals, as depicted in the Equations 1 and 2, respectively. Under oxidizing conditions:

$$E_{doping} = E^{Se}[Mn_{24}Na_6Li_6O_{60}] - E[Mn_{24}Na_6Li_6O_{60}0] - \mu_{MnO2/Na2O/Li2O/O} - \mu_{SeO2} \quad (1)$$

Under reducing conditions:

$$E_{doping} = E^{Se}[Mn_{24}Na_6Li_6O_{60}] - E[Mn_{24}Na_6Li_6O_{60}0] - \mu_{Mn/Na/Li/O} - \mu_{Se} \quad [2]$$

The oxygen dimer formation energy was computed using the following equation:

$$E_{O\text{-}O\ Dimer\ formation} = E_{O2\ vacant} - E_{pristine} - 2\mu_O \quad [3]$$

The most stable phases of metals under the reaction conditions are used, and the chemical potential of the oxygen is corrected relative to Enthalpy of water at 300K using the following equation: $\mu_O = E_{H2O} - E_{H2}$ - 2.506 eV. This amounts for difference in $\mu_O$ of +0.19 eV per O atom. Lastly, the chemical potential of oxygen under reducing conditions[41] is further adjusted by -0.98 eV, corresponding to a pressure of 1 atm and a temperature of 900 K.

**References**


1. C. Vaalma, D. Buchholz, M. Weil, S. Passerini, Nat. Rev. Mater. **2018**,3, 18013
2. R. Usiskin, Y. Lu, J. Popovic, M. Law, P. Balaya, Y.-S. Hu, Nat. Rev. Mater. **2021**, 6, 1020-1035.
3. K. Du, J. Zhu, G. Hu, H. Gao, Y. Li, J. B. Goodenough, Exploring reversible oxidation of oxygen in a manganese oxide. Energy Environ. **2016**, Sci. 9, 2575-2577.

4. X. Rong, J. Liu, E. Hu, Y. Liu, Y. Wang, J. Wu, X. Yu, K. Page, Y.-S. Hu, W. Yang, H. Li, X.-Q. Yang, L. Chen, X. Huang, Structure-Induced Reversible Anionic Redox Activity in Na Layered Oxide Cathode. Joule **2018**,2, 125-140.
5. A. Gao, Q. Zhang, X. Li, T. Shang, Z. Tang, X. Lu, Y. Luo, J. Ding, W. H. Kan, H. Chen, W. Yin, X. Wang, D. Xiao, D. Su, H. Li, X. Rong, X. Yu, Q. Yu, F. Meng, C. Nan, C. Delmas, L. Chen, Y.-S. Hu, L. Gu, Nat. Sustainability **2022**, 5, 214-224.
6. Y. Tang, Q. Zhang, W. Zuo, S. Zhou, G. Zeng, B. Zhang, H. Zhang, Z. Huang, L. Zheng, J. Xu, W. Yin, Y. Qiu, Y. Xiao, Q. Zhang, T. Zhao, H. Liao, I. Hwang, C. Sun, K. Amine, Q. Wang, Y. Sun, G. Xu, L. Gu, Y. Qiao, S. Sun, Nat. Sustainability 2022, 5, 214–224
7. K. Dai, J. Wu, Z. Zhuo, Q. Li, S. Sallis, J. Mao, G. Ai, C. Sun, Z. Li, W. E. Gent, W. C. Chueh, Y.-d. Chuang, R. Zeng, Z.-x. Shen, F. Pan, S. Yan, L. F. J. Piper, Z. Hussain, G. Liu, W. Yang, Joule **2019**, 3, 518-541.
8. W. E. Gent, I. I. Abate, W. Yang, L. F. Nazar, W. C. Chueh, Joule **2020**, 4, 1369-1397.
9. R. A. House, U. Maitra, M. A. Pérez-Osorio, J. G. Lozano, L. Jin, J. W. Somerville, L. C. Duda, A. Nag, A. Walters, K.-J. Zhou, M. R. Roberts, P. G. Bruce,Nature, **2020**,577, 502-508.
10. Z.-C. Xue, J.-n. Huang, X. Guo, H. Guo, Y. Zhu, G.-r. Hu, Z.-d. Peng, Y.-b. Cao, K. Du, Ceram. Int. **2022**, 48, 25642-25646.
11. E. Hu, X. Yu, R. Lin, X. Bi, J. Lu, S. Bak, K.-W. Nam, H. L. Xin, C. Jaye, D. A. Fischer, K. Amine, X.-Q. Yang, Nat. Energy **2018**, 3, 690-698.
12. M. Saubanère, E. McCalla, J. M. Tarascon, M. L. Doublet, Energy Environ. Sci. **2016**, 9, 984-991.
13. H. Ren, Y. Li, Q. Ni, Y. Bai, H. Zhao, C. Wu, Advanced Materials 2022, 34, 2106171. Adv. Mater. **2022**, 34, 2106171.
14. X. Zhang, Y. Qiao, S. Guo, K. Jiang, S. Xu, H. Xu, P. Wang, P. He, H. Zhou, Adv. Mater. **2019**, 31, 1807770.
15. Y. Wang, X. Zhao, J. Jin, Q. Shen, Y. Hu, X. Song, H. Li, X. Qu, L. Jiao, Y. Liu, J. Am. Chem. Soc **2023**, 145, 22708.

16. L. Yao, P. Zou, C. Wang, J. Jiang, L. Ma, S. Tan, K. A. Beyer, F. Xu, E. Hu, H. L. Xin, Adv. Energy Mater. **2022**, 12, 2201989.
17. H. Ji, W. Ji, H. Xue, G. Chen, R. Qi, Z. Huang, H. Fang, M. Chu, L. Liu, Z. Ma, S. Xu, J. Zhai, W. Zeng, C. Schulz, D. Wong, H. Chen, J. Xu, W. Yin, F. Pan, Y. Xiao Sci. Bull. **2023**, 68, 65-76.
18. C. Yan, Q. Shao, Y. Yang, M. Gao, Y. Lin, M. Gao, Z. Chen, Y. Wei, Y. Liu, W. Sun, Y. Jiang, X. Zhang, J. Chen, Z. Wu, H. Pan Adv. Funct. Mater. 2024, 34, 2310873.
19. B. Su, J. Zhang, M. Fujita, W. Zhou, P. H. L. Sit, D. Y. W. Yu, J. Electrochem. Soc. **2019**, 166, A5075.
20. Z. Zhu, H. Wang, Y. Li, R. Gao, X. Xiao, Q. Yu, C. Wang, I. Waluyo, J. Ding, A. Hunt, J. Li, Adv. Mater. **2020**, 32, 2005182.
21. C. Delmas, C. Fouassier, P. Hagenmuller, Physica B+C 1980, 99, 81.
22. H. Yu, A. Gao, X. Rong, S. Shen, X. Zheng, L. Yan, H. Wang, D. Su, Z. Hu, W. H. Kan, H. Chen, W. Yin, Y. Lu, Q. Zhang, L. Gu, C. Delmas, L. Chen, S. Wang, Y.-S. Hu, Energy Environ. Sci., **2024**,17, 3855-3867.
23. E. de la Llave, E. Talaie, E. Levi, P. K. Nayak, M. Dixit, P. T. Rao, P. Hartmann, F. Chesneau, D. T. Major, M. Greenstein, D. Aurbach, L. F. Nazar, Chem. Mater. **2016**, 28, 9064.
24. C. Tian, D. Nordlund, H. L. Xin, Y. Xu, Y. Liu, D. Sokaras, F. Lin, M. M. Doeff, J. Electrochem. Soc **2018**,165, A696.
25. F. Lin, Y. Liu, X. Yu, L. Cheng, A. Singer, O. G. Shpyrko, H. L. Xin, N. Tamura, C. Tian, T.-C. Weng, X.-Q. Yang, Y. S. Meng, D. Nordlund, W. Yang, M. M. Doeff, Chem. Rev. **2017**, 117, 13123.
26. J. Wu, Y. Yang, W. Yang, Dalton Trans. **2020**, 49, 13519.
27. S. Tan, D. Kuai, Z. Yu, S. Perez-Beltran, M. M. Rahman, K. Xia, N. Wang, Y. Chen, X.-Q. Yang, J. Xiao, J. Liu, Y. Cui, Z. Bao, P. B. Balbuena, E. Hu, J. Am. Chem. Soc **2024**,146, 11711.
28. N. Zhang, G. Ren, L. Li, Z. Wang, P. Yu, X. Li, J. Zhou, H. Zhang, L. Zhang, Z. Liu, X. Liu, Nat. Commun. **2024**, 15, 2777
29. R. Qiao, Y.-D. Chuang, S. Yan, W. Yang, PLOS ONE **2012**, 7, e49182.
30. H. Hu, H.-C. He, R.-K. Xie, C. Cheng, T. Yan, C. Chen, D. Sun, T.-S. Chan, J. Wu, L. Zhang, Nano Energy **2022**, 99, 107390.

31. A. Grimaud, W. T. Hong, Y. Shao-Horn, J. M. Tarascon, Nat. Mater. **2016**, 15, 121
32. P. E. Pearce, A. J. Perez, G. Rousse, M. Saubanère, D. Batuk, D. Foix, E. McCalla, A. M. Abakumov, G. Van Tendeloo, M.-L. Doublet, J.-M. Tarascon, Nat. Mater. **2017**, 16, 580.
33. M. Sathiya, G. Rousse, K. Ramesha, C. P. Laisa, H. Vezin, M. T. Sougrati, M. L. Doublet, D. Foix, D. Gonbeau, W. Walker, A. S. Prakash, M. Ben Hassine, L. Dupont, J. M. Tarascon, Nat. Mater. **2013**, 12, 827-835.
34. B. Kim, J.-H. Song, D. Eum, S. Yu, K. Oh, M. H. Lee, H.-Y. Jang, K. Kang. Nat. Sustainability **2022**, 5, 708-716.
35. F. Meirer, J. Cabana, Y. Liu, A. Mehta, P. Pianetta,J. Synchrotron Radiat. **2011**, 18, 773.
36. Yijin, Liu, Florian, Meirer, Phillip, A., Williams, Junyue, Wang, Joy, J. Synchrotron Radiat. **2012**, 19,281-287.
37. G. Kresse, J. Furthmüller, Phys. Rev. B **1996**, 54, 11169.
38. G. Kresse, D. Joubert, Phys. Rev. B**1999**, 59, 1758.
39. H. J. Monkhorst, J. D. Pack, Phys. Rev. B **1976**, 13, 5188.
40. I. A. Vladimir, F. Aryasetiawan, A. I. Lichtenstein, J. Phys.: Condens. Matter **1997**, 9, 767.
41. K. Reuter, M. Scheffler, Phys. Rev. B. **2001,** 65, 035406.

**Acknowledgments**

This work was supported by the U.S. Department of Energy (DOE), Office of Basic Energy Sciences, Division of Materials Sciences and Engineering (Contract No. DE-AC02-76SF00515). Use of the Stanford Synchrotron Radiation Lightsource, SLAC National Accelerator Laboratory, is supported by the U.S. Department of Energy (DOE), Office of Science, Office of Basic Energy Sciences. Part of this work was performed at the Stanford Nano Shared Facilities (SNSF), supported by the National Science Foundation under award ECCS-1542152. We would like to acknowledge Dr. Penghao Chen from Institute of Physics, Chinese Academy of Sciences for the fruitful X-ray diffraction discussion. N.B. and M.B. were supported by the U.S. Department of Energy, Office of Science, Office of Basic Energy Sciences, Chemical

Sciences, Geosciences, and Biosciences Division, Catalysis Science Program to the SUNCAT Center for Interface Science and Catalysis. SUNCAT-FWP: This research used resources of the National Energy Research Scientific Computing Center, a DOE Office of Science User Facility supported by the Office of Science of the U.S. Department of Energy under Contract No. DE-AC02-05CH11231 using NERSC award BES-ERCAP0024127. Dr. Zhichen Xue extends his heartfelt gratitude to Central South University for the technical support and mentorship received throughout his Ph.D. journey.

**Author Contributions:** X.Z., J.N., and M.B. supervised the work. X.Z., J.N., and Z.X. conceived the research concept and designed experiments. Z.X. conducted the materials synthesis, electrochemistry, and cell performance. Z.X. and Y.L. conducted the TXM experiments and related data analysis. Z.X. and S.L. conducted the XAS experiments and conducted the analysis. Z.X., T. C., H. H. conducted the XRD and XPS experiments. G.F., Y.L., T.C., and D.M. conducted the TEM and SEM experiments and related data analysis. M.B. and N.B. conducted the theoretical calculation and related data analysis. All authors discussed the results, co-wrote, and commented on the manuscript.

**Competing declarations:** The authors declare they have no competing interests.

**Data and materials availability:** All data needed to evaluate the conclusions in the paper are present in the paper and/or the Supplementary Materials. The adsorption energy data set are available at www.catalysis-hub.org/publications/BothraSodium2024.db.

**Corresponding authors**

Correspondence to Michal Bajdich (bajdich@slac.stanford.edu)；Jagjit Nanda (jnanda@slac.stanford.edu); Xueli Zheng(xuelizh8@stanford.edu).

# Supplementary Materials for

## Coupling Anionic Oxygen Redox with Selenium for Stable High-voltage Sodium Layered Oxide Cathodes

Zhichen Xue [a], Neha Bothra [b], Dechao Meng [a], Guangxia Feng [c], Yuqi Li [c], Tony Cui [c], Hongchang Hao [d], Sang-Jun Lee [a], Yijin Liu [e], Michal Bajdich [b,*], Jagjit Nanda [c,d,*], Xueli Zheng [c,d*]

[a.] Stanford Synchrotron Radiation Lightsource, SLAC National Accelerator Laboratory, Menlo Park, CA, USA

[b.] SUNCAT Center for Interface Science and Catalysis, SLAC National Accelerator Laboratory, Menlo Park, CA, USA

[c.] Materials Science and Engineering, Stanford University, Stanford, California 94305, USA

[d.] Applied Energy Division, SLAC National Laboratory, Menlo Park, CA, USA

[e.] Walker Department of Mechanical Engineering, The University of Texas at Austin, Austin, TX, USA

*Corresponding author. Email: xuelizh8@stanford.edu, jnanda@slac.stanford.edu, bajdich@slac.stanford.edu

**This PDF file includes:**

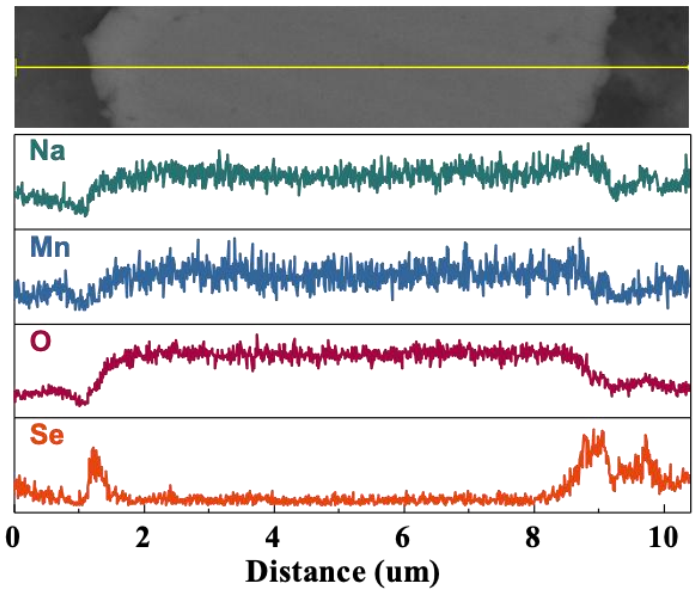


**Fig. S1.** Cross section scanning electron microscopy and energy-dispersive X-ray spectroscopy element line scan profile of Na, Mn, O and Se.

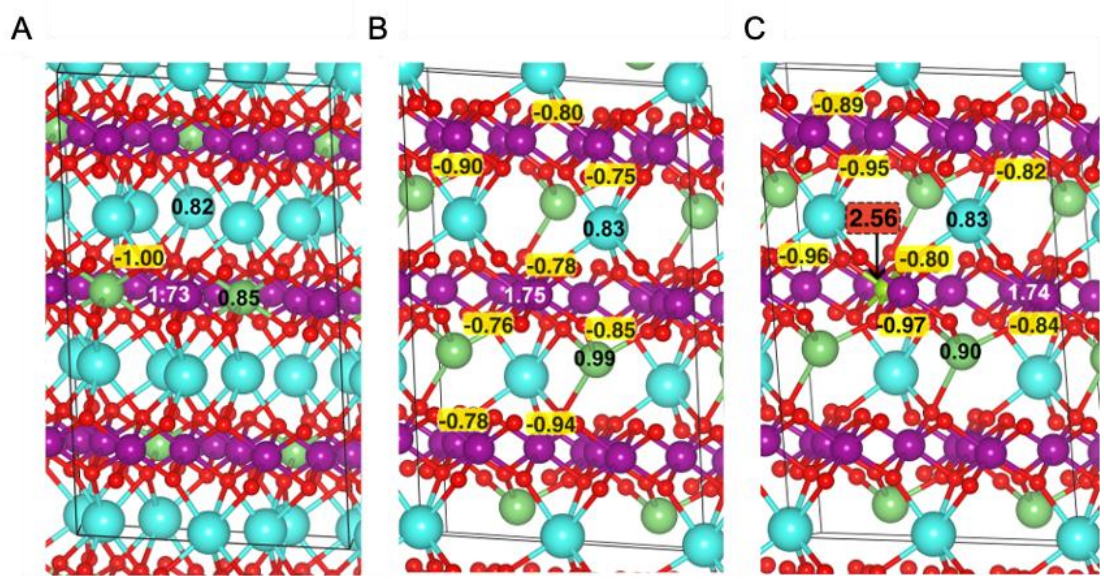


**Fig. S2.** Bader charge analysis for three different NLMO systems: (A) undoped discharged, (B) undoped charged, and (C) selenium-doped at the manganese site in the charged state. For Mn atoms, the Bader charge remains constant around 1.7e$^-$, indicating a +4 oxidation state. The Bader charges for Na and Li atoms are also consistent, around ~0.84e$^-$, corresponding to a +1 oxidation state. In the transition from the discharged to the charged state, oxygen atoms show a change in Bader charge from -1.0e$^-$ to approximately -0.9e$^-$, highlighted with a yellow background. The selenium atom in the charged state shows a Bader charge indicating a formal oxidation state of approximately 5.2, marked with red highlights. Bader charges for Na, Li, and O are shown in black fonts, while those for Mn are displayed in white font.

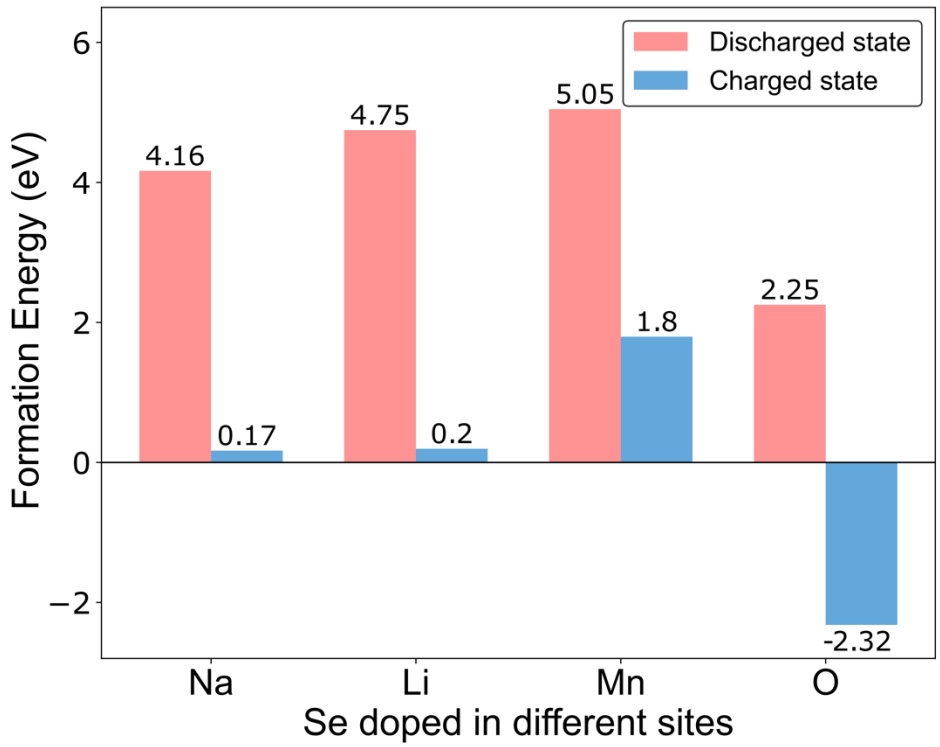


**Fig. S3.** Energetics of selenium substitution scenarios under reducing conditions for discharged (salmon) and charged state (cyan), similar to **Fig. 2E**.

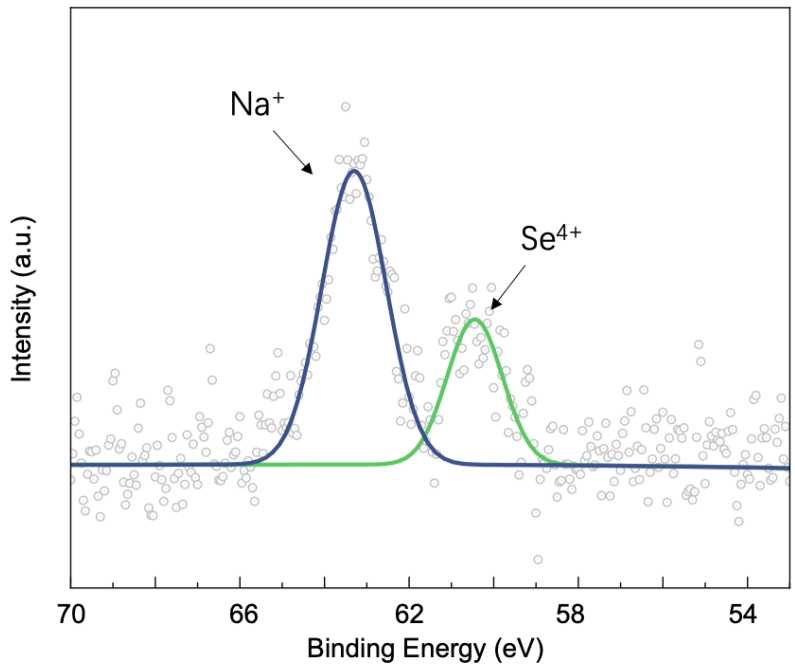


**Fig. S4.** The X-ray photoelectron spectroscopy investigation for as-prepared NLMO-Se.

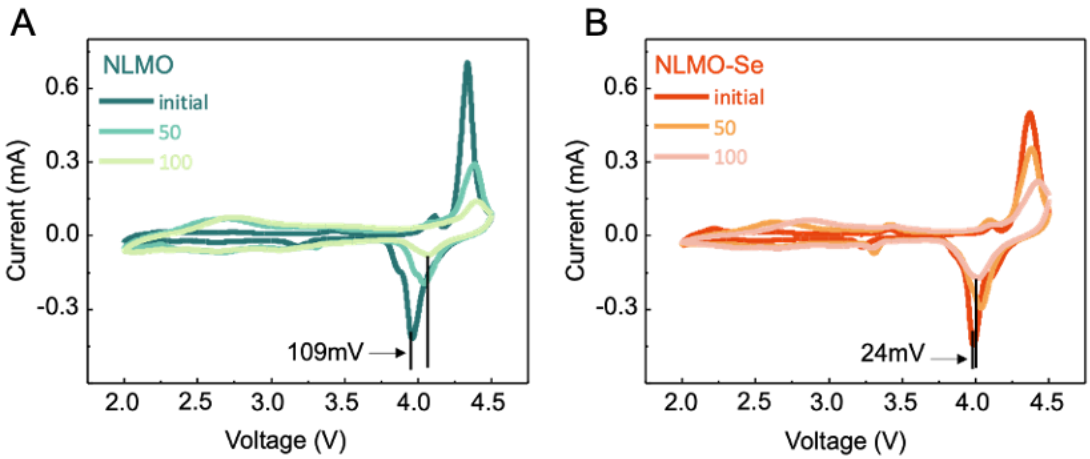


**Fig. S5.** Cyclic voltammetry curves for NLMO(A) and NLMO-Se(B) during cycling in the voltage range of 2-4.5V for the initial, 50$^{th}$, and 100$^{th}$ cycles.

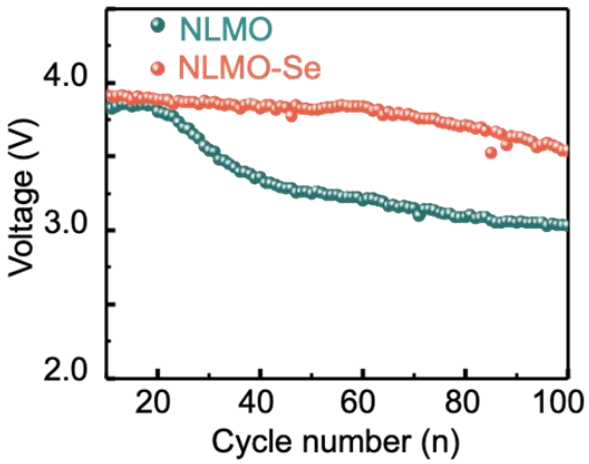


**Fig. S6.** Variation of the middle discharge voltage of NLMO and NLMO-Se during cycles undering the current of 100 mA/g)

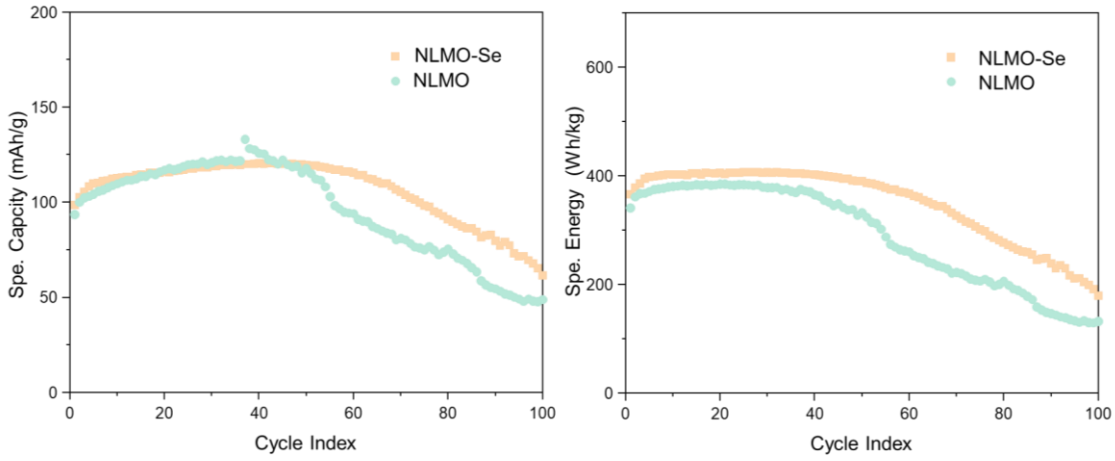


**Fig. S7.** Specific capacity (left) and specific energy (right) decay trends of NLMO and NLMO-Se at a current of 25 mA/g.

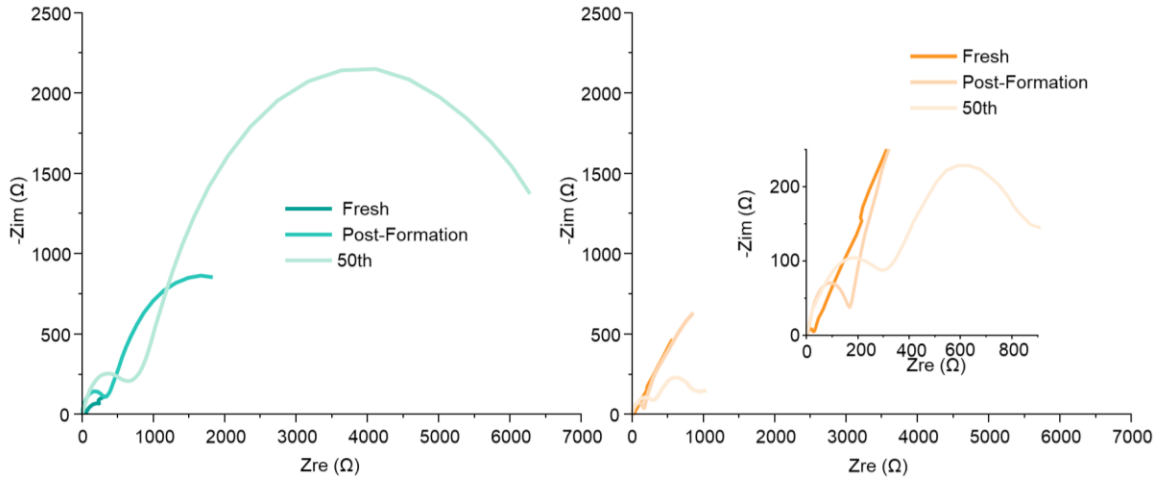


**Fig. S8.** Electrochemical impedance spectra of fresh, post-formation, and cycled LNMO (left) and NLMO-Se(right).

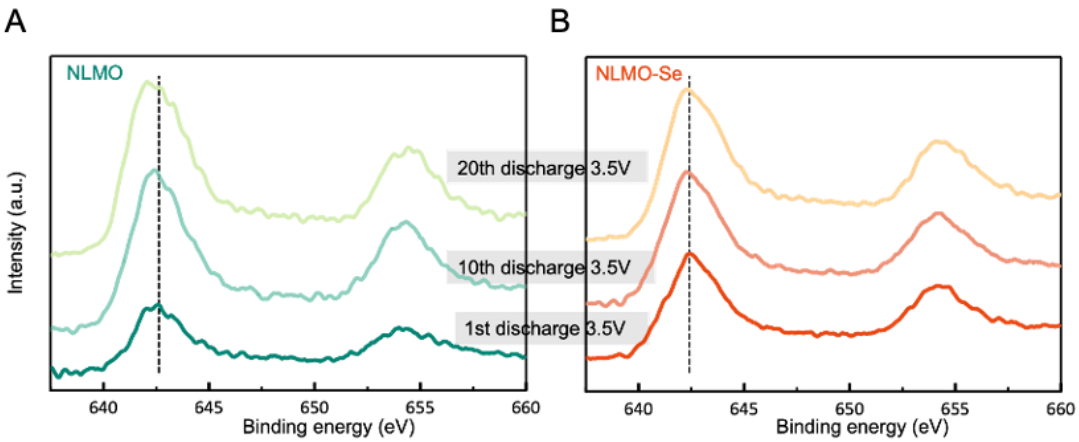


**Fig. S9.** The X-ray photoelectron spectroscopy Mn 2p fingerprint spectra for the NLMO(A) and NLMO-Se(B) are abused under only oxygen redox charge-discharge protocol (3.5-4.5V) at different cycles.

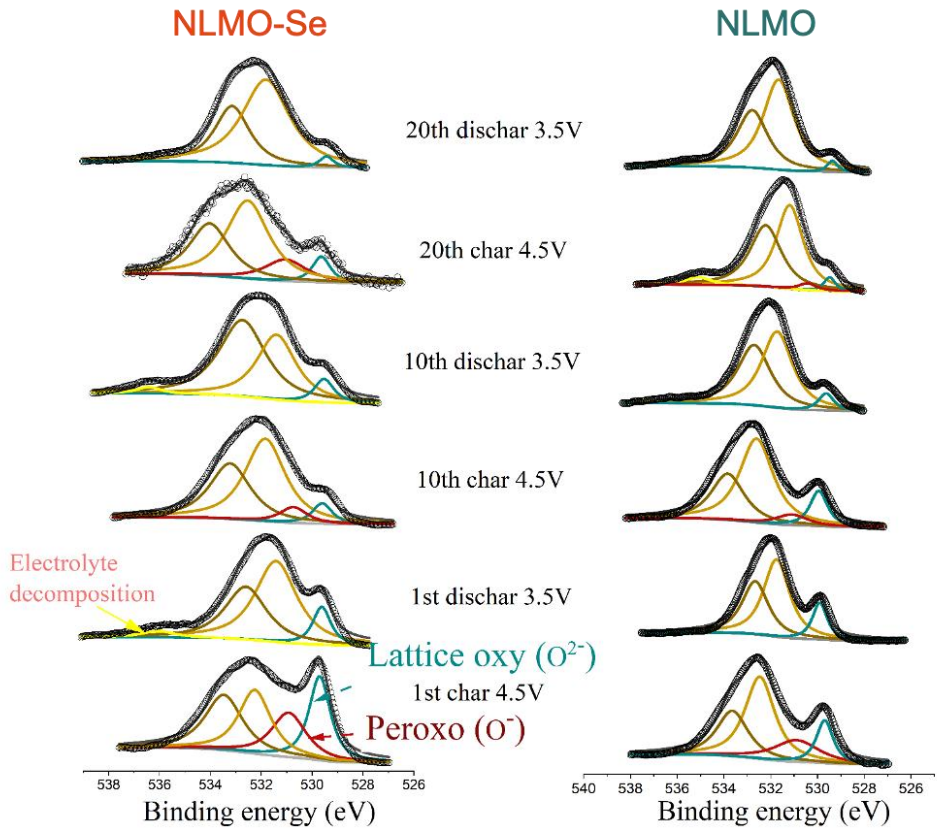


**Fig. S10.** O1s X-ray Photoelectron Spectroscopy for the NLMO and NLMO-Se at different states of charge.

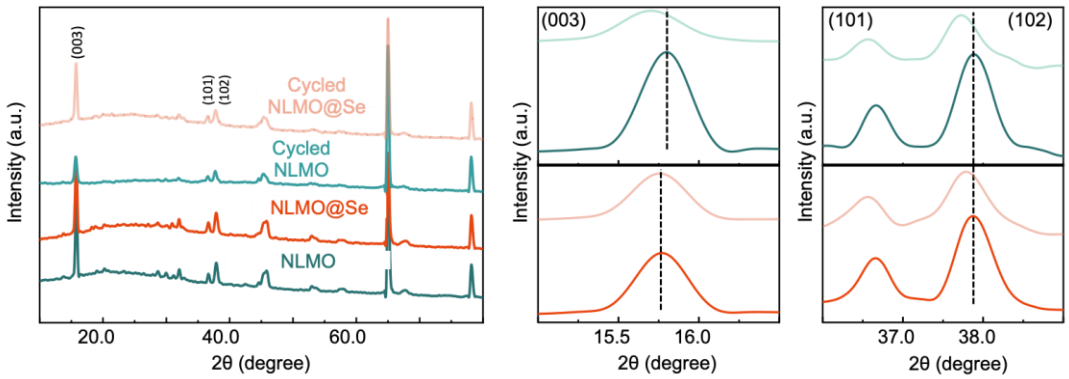


**Fig. S11.** The XRD pattern for NLMO and NLMO-Se at the pristine state and after 50 cycles. The NLMO peaks of (003) and (102) shift to a lower angle after cycling.

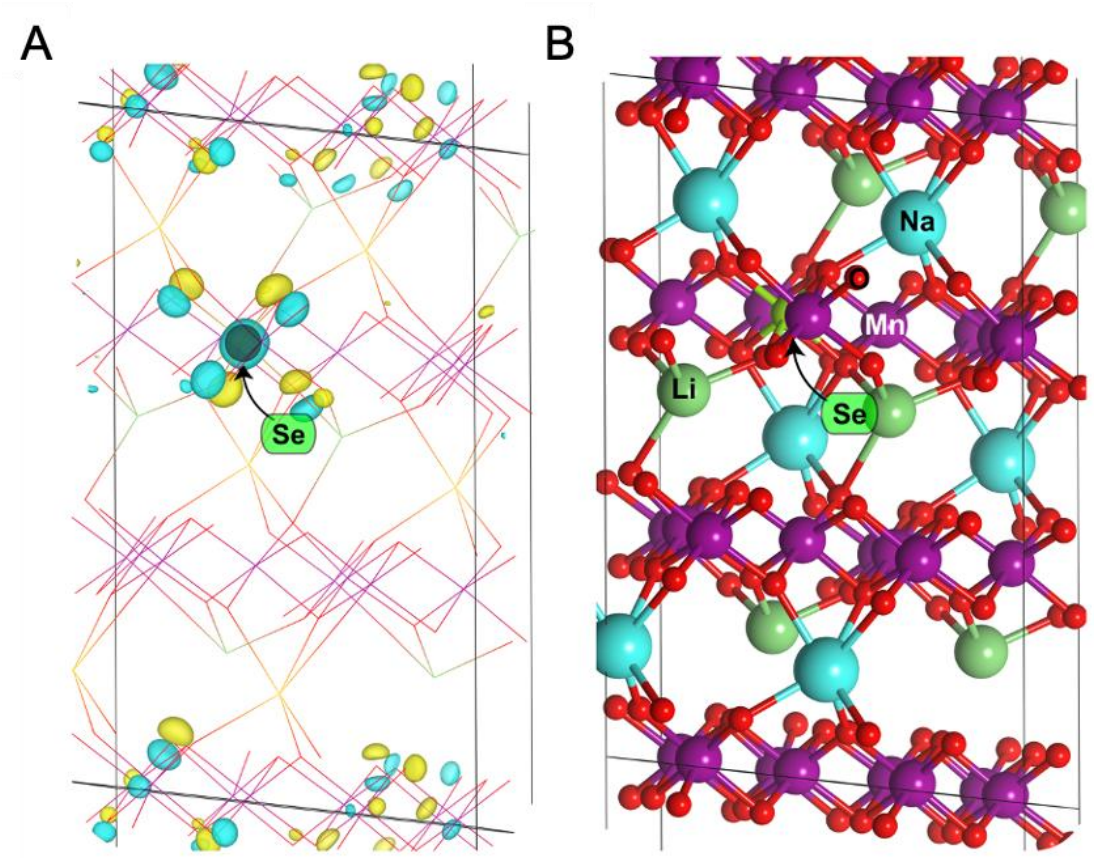


**Fig. S12.** A, Charge density difference analysis for the NLMO-Se and NLMO systems revealing regions of charge accumulation and depletion. The yellow and cyan surfaces represent areas where charge has accumulated and depleted, respectively (surface isovalues were set to +/- 0.015 e/Å³). The charge effect is the largest at adjacent oxygen atoms. The dark grey shaded region indicates the presence of extra core electron of Se

atom vs. Mn atom. B, Crystal Lattice structure of the NLMO-Se system and the doped atom.

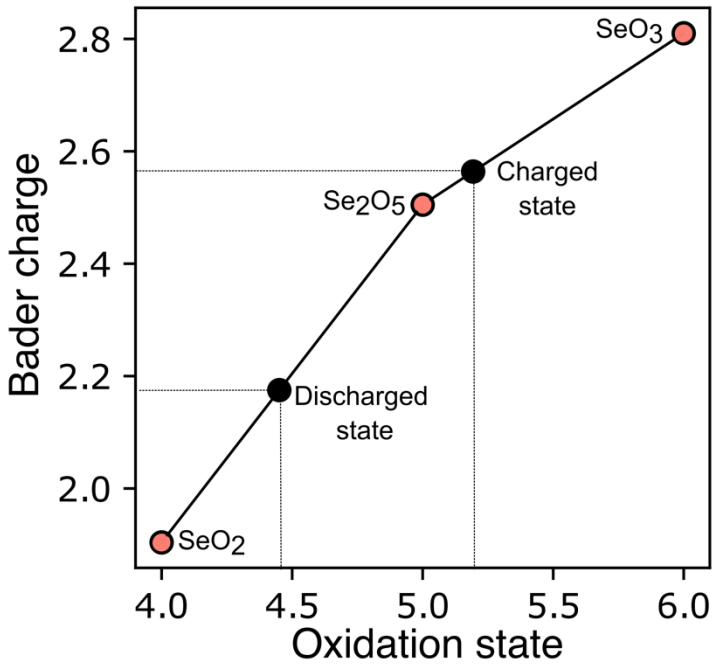


**Fig. S13. Comparison of the computed Bader charges and formal oxidation states of Se compounds.** Orange circle represents the Bader charge values of $SeO_2$ (+4), $Se_2O_5$ (+5) and $SeO_3$ (+6). The pure Se oxides are connected with black solid line and we can analyze the formal oxidation state with provided Bader charge. The formal oxidation state of Se in Se-doped NLMO in the charged and discharged states is represented by the black circle, which shows oxidation of Se from 4.4 to 5.2 respectively from the discharged to charged state. The dashed black lines point in the same direction.

**Table S1.** Calculated formation energies for Se-doped systems in discharged and charged states under oxidizing conditions used in **Figures 2E** and **S3**. The listed values compare free energy calculations ($\Delta G$) as described in Methods Section with raw electronic energies from Catalysis-Hub.org ($\Delta E$). In Catalysis-Hub.org values, the raw electronic energy of the uncorrected oxygen molecule is used, which is -0.29 eV more negative per O atom. Under reducing conditions, the chemical potential of oxygen is additionally modified by -0.98 eV to account for a pressure of 1 atm and a temperature of 900 K (41). The full adsorption energy dataset and including geometries are available at www.catalysis-hub.org/publications/ BothraSodium2024.db.

| Se Doped | ΔG Discharged System (eV) | $\Delta E$ Discharged System (Catalysis-hub.org) (eV) | ΔG Charged System (eV) | $\Delta E$ Charged System (Catalysis-hub.org) (eV) |
|---|---|---|---|---|
| Na | 4.78 | 4.35 | 0.78 | 0.35 |
| Li | 4.47 | 4.04 | -0.09 | -0.52 |
| Mn | 2.38 | 2.38 | -0.87 | -0.87 |
| O | 5.88 | 5.02 | 1.31 | 0.45 |
| O (900K) | 2.25 | 2.94 | -2.32 | -1.63 |

**Table S2.** Calculated oxygen dimer formation energies for undoped and Se-doped charged systems from Figure 5. Same as in **Table S1**, Catalysis-Hub.org values use the raw electronic energy of the uncorrected oxygen molecule is used, which is -0.29 eV more negative per O atom.

| | ΔG (Undoped) (eV) | ΔE (Undoped) (Catalysis-hub.org) (eV) | ΔG (Doped) (eV) | ΔE (Doped) (Catalysis-hub.org) (eV) |
|---|---|---|---|---|
| Pair 1 | 1.25 | 0.68 | 2.11 | 1.54 |
| Pair2 | 1.80 | 1.23 | 2.09 | 1.52 |
| Pair 3 | 1.96 | 1.38 | 2.06 | 1.49 |
| Pair 4 | 1.69 | 1.12 | 2.41 | 1.83 |
| Pair 5 | 1.98 | 1.40 | 2.74 | 2.17 |

**Table S3.** Comparison of electrochemical performance of NLMO-Se samples and NLMO with different selenium doping levels in the 3.5–4.5V (25 mAh/g)

| | First Discharge Capacity (mAh/g) | $50^{th}$ Discharge Capacity (mAh/g) | Capacity Rentention |
|---|---|---|---|
| NLMO | 71 | 27.7 | 39.02% |
| NLMO-Se (0.5%) | 68.4 | 53.3 | 77.97% |
| NLMO-Se(1%) | 62.3 | 52.2 | 83.86% |
| NLMO-Se(1.5%) | 67.2 | 25.6 | 67.81% |